

Detection of chiral anomaly and valley transport in Dirac semimetals

Cheng Zhang^{1,2}, Enze Zhang^{1,2}, Yanwen Liu^{1,2}, Zhi-Gang Chen^{3*}, Sihang Liang^{1,2},
Junzhi Cao^{1,2}, Xiang Yuan^{1,2}, Lei Tang^{1,2}, Qian Li^{1,2}, Teng Gu^{1,2}, Yizheng Wu^{1,2}, Jin
Zou^{3,4*}, Faxian Xiu^{1,2*}

¹ State Key Laboratory of Surface Physics and Department of Physics, Fudan University,
Shanghai 200433, China

² Collaborative Innovation Center of Advanced Microstructures, Fudan University,
Shanghai 200433, China

³ Materials Engineering, The University of Queensland, Brisbane QLD 4072, Australia

⁴ Centre for Microscopy and Microanalysis, The University of Queensland, Brisbane
QLD 4072, Australia

* Correspondence and requests for materials should be addressed to F. X. (E-mail: faxian@fudan.edu.cn), J. Z. (Email: j.zou@uq.edu.au) and Z-G. C. (Email: z.chen1@uq.edu.au)

Abstract

Chiral anomaly is a non-conservation of chiral charge pumped by the topological nontrivial gauge field. As an analogy to the similar phenomenon in high-energy physics, the chiral anomaly in condensed matter is predicted to exist in the emergent quasiparticle excitations in Dirac and Weyl semimetals. However, the current understanding of such concept mostly remains in the theoretical consideration, which lacks of convincing experimental identification. Here, for the first time, we experimentally observe the existence of the chiral anomaly and the related valley transport in Cd_3As_2 . We find that the chiral imbalance induced by external electric and magnetic fields ($\mathbf{E} \cdot \mathbf{B}$) leads to a non-zero gyrotropic coefficient γ , which can be confirmed by the $\mathbf{E} \cdot \mathbf{B}$ -generated Kerr effect. By applying \mathbf{B} along the current direction, we observe a negative magnetoresistance despite the giant positive one at other directions, a clear indication of the chiral anomaly. Remarkably, a robust nonlocal response from valley diffusion originated from the chiral anomaly is observed up to room temperature when \mathbf{B} is parallel to \mathbf{E} . Our discovery of the chiral anomaly in Cd_3As_2 Dirac semimetal opens up a brand-new route to understand its fundamental properties with a controllable chiral imbalance through external fields and utilize the chiral fermions in valleytronic applications.

Conservation laws arising from preserved symmetries are the base of modern physics (1). However, when a classically preserved symmetry is broken upon quantization, such conservation may encounter a so-called quantum anomaly (2). The chiral anomaly, one of the typical examples, manifests itself in non-conservation of chiral charge induced by topological nontrivial gauge fields (2, 3). As a long-pursued topic in quantum field theory context, Weyl fermions host definite chiral charges with opposite signs (2), whose chirality is defined by the sign of its spin polarization along the momentum direction. Weyl fermions with different chiralities are independently coupled to different chiral gauge fields, resulting in a separate charge conservation (2, 4). Thus, in the presence of chiral gauge field, Weyl fermions possess a non-conserved chiral charge, *i.e.*, the chiral anomaly.

Despite its crucial role in the description of elementary particles, the study of Weyl fermions in condensed matter physics has only been paid intensive attention in recent years (5-7). The condensed matter analogy of Weyl fermions was proposed as the emergent quasiparticle excitations of certain novel gapless topological matter, which is named as “Weyl semimetal” (4). In a Weyl semimetal, the band structure shows semimetal behavior with the conduction and valence bands intersecting only at some discrete points, denoted as Weyl nodes (4, 6). A non-zero Chern number is expected to emerge when the Fermi surface encloses a Weyl node, which can be viewed as a Berry curvature singular point (2, 4). With time-reversal and inversion symmetries preserved, the Dirac nodes can be formed by two degenerated Weyl nodes, driving the system into a Dirac semimetal, a close sibling of the Weyl semimetal (8). In Dirac semimetals, these

nodes with opposite chiralities are distinguished by the point-group index or isospin (9).

Typically, additional crystalline point-group symmetry is required to prevent the overlapping of the Weyl nodes with different chiralities from annihilation (8, 9). As the

Weyl nodes are topologically-protected objects with defined chirality, the Dirac/Weyl

semimetals are predicted to harbor many exotic effects, such as surface Fermi arc states

(5) and axion strings (10). Among them, the chiral anomaly raises particular interests owing to its important role in the 4-dimensional quantum Hall boundary state (11).

Furthermore, the chiral anomaly promises many intriguing transport phenomena, such as negative magnetoresistance (MR) (12), anomalous Hall effect (13) and nonlocal valley transport (14), holding prospects in valleytronics.

After several years exploring the existence of Weyl fermions in crystalline solids, Na_3Bi and Cd_3As_2 have been theoretically predicted and experimentally confirmed as Dirac semimetals (9, 15-19). Photoemission spectroscopy has unveiled the degenerated Weyl nodes (16, 18, 19) (Dirac nodes) and spin-polarized Fermi arc surface states (20) in these Dirac semimetals. Ultra-high mobility and giant linear MR in Cd_3As_2 have drawn extensive attentions, aiming to understanding its transport properties and physical origin (21). Magnetic-field induced phase transition in Cd_3As_2 provides signatures for the isolation of Weyl nodes with time-reversal symmetry broken (22). However, so far no unambiguous experimental evidence has been provided to confirm the chiral anomaly in these materials. Owing to the intrinsic vacancies, both Na_3Bi and Cd_3As_2 possess relatively high Fermi levels and the chiral magnetic effect is consequently weakened. Thus, accompanied by the large positive MR as the

background, the anticipated negative MR is challenging to be detected. Hence, the priority in the field of the Dirac/Weyl semimetals is to unambiguously confirm the chiral anomaly with new and reliable approaches.

Here, we demonstrate the existence of the chiral anomaly in Cd₃As₂ based on three independent experimental evidences: the E·B-generated magneto-optical Kerr effect (MOKE), the negative MR, and the valley transport. It is well known that the degenerated Weyl nodes in Cd₃As₂ adopt opposite chirality, which can be coupled with external electromagnetic fields (6, 23). In the presence of parallel electric and magnetic fields, electrons can be pumped from one node to the other. Such a pumping process will be compensated by the depletion of chiral charge from inter-valley diffusion. Eventually, the Weyl nodes with opposite chirality χ will acquire a different chemical potential as schematically illustrated in Fig. 1A. This chirality-dependent chemical potential can be presented by (5),

$$\mu_\chi = \chi \left(\frac{3e^2 \hbar v_F^3}{2} \mathbf{E} \cdot \mathbf{B} \tau_v \right)^{1/3}, \quad (1)$$

where e is the electron charge, v_F is Fermi velocity, \mathbf{E} and \mathbf{B} are the external electric and magnetic fields, and τ_v is the inter-valley scattering time. It has been proposed that the charge imbalance between the Weyl nodes leads to a non-zero gyrotropic coefficient γ , a Hall-like contribution to the dielectric tensor (23). For a single Weyl node, γ is given by (23): $\gamma(\omega) = i \frac{\chi \mu_\chi e^2 \tau_{intra}}{6\pi^2 \epsilon_0 \hbar^2 \omega}$ with ω being the light frequency and τ_{intra} being the intra-valley scattering time. Note that this extra γ is purely imaginary so that it leads to circular dichroism.

In order to detect γ , we carried out rotating-of-field magneto-optical Kerr effect (ROTMOKE) measurements on the bulk Cd_3As_2 single crystals. A 2-dimensional vector rotate magnet is used to generate a rotating magnetic field in the y-z plane, which is parallel to the sample surface as illustrated in Fig. 1B. In the MOKE measurements, the Kerr rotation angle from a *p*-polarized light can be quantified as a function of field strength and orientations (24). Initially, no Kerr signals from the crystal surface were observed, as one can expect from a system with preserved inversion and time-reversal symmetries. However, when an electric bias was applied on the two ends of the samples, the large Kerr rotation signals were dramatically produced with increasing the bias voltage (0~500 mV), as demonstrated in Fig. 1C. Fig. 1D shows the ROTMOKE data under different magnetic fields with a fixed bias of 500 mV. The ROTMOKE curve adopts a cosine-function dependence on the angle θ between the electric and magnetic fields. The absolute value of Kerr rotation reaches a maximum when the electric and magnetic fields are parallel ($\theta = 0$), and in turn it becomes zero when they are perpendicular ($\theta = 90^\circ$). This angular dependence is in good agreement with the chiral gauge field $\mathbf{E} \cdot \mathbf{B}$ which we use for the charge pumping in this study. In addition, we performed the ROTMOKE experiments with the magnetic field in the x-z plane (fig. S2). When the electric field is parallel to the B-rotating plane, the similar 360 °-period ROTMOKE curves were observed (fig. S2B). However, when the bias was added perpendicularly to the B-rotating plane, no Kerr signal was ever detected (fig. S2D) due to the vanishing of $\mathbf{E} \cdot \mathbf{B}$. This $\mathbf{E} \cdot \mathbf{B}$ term induced Kerr effect serves as a consolidate proof for the emerging chiral charge under external gauge fields.

Besides the influence on the optical properties, the chiral anomaly can also be detected through the electric transport. One important signature of the chiral anomaly is the large negative MR with unusual anisotropy with respect to the angle between **E** and **B** (12). To investigate the transport properties, we fabricated Hall bar devices based on Cd₃As₂ nanoplates. These nanostructures were grown by chemical vapor deposition method (detailed information of growth and material characterizations can be found in the section V of the supplementary material). The magnetotransport properties of Cd₃As₂ nanoplates were systematically studied in our previous work (25). It has been demonstrated that Cd₃As₂ transforms into semiconductors when approaching two-dimensional limit. Here we specifically chose thick nanoplates (~ 90 nm) to ensure their semimetallic properties. Fig. 2A summarizes the angle-dependent MR of the Cd₃As₂ nanoplates at 2.5 K. As illustrated in Fig. 2A inset, **B** was rotated from in-plane to out-of-plane with θ defined as the angle between **B** and the applied current **I**. A large positive and linear MR along with a strong anisotropy respective to the field direction was obtained, similar to those observed in Cd₃As₂ bulk crystals (refer to fig. S4A). Remarkably, by carefully investigating the MR behavior as **B** approaches **I**, we find a clear dip emerging in the MR curve, which vanishes rapidly even if θ changes only a few degrees (Fig. 2B). Owing to its large amplitude and the corresponding field range (-2~2 T), this dip is distinct from the weak-localization or the SdH oscillations. For the magnetic field over 2 T, the MR turns upwards, very similar to that in Bi_{1-x}Sb_x (26).

To exclude the influence from the intrinsic crystal anisotropy, we designed three different geometries to conduct transport measurements as shown in Fig. 2C left panel.

The dip and the strongly suppressed MR trend disappear as long as \mathbf{B} and \mathbf{I} are not parallel (Fig. 2C right panel). Our control experiments suggest that the detected negative MR originates from the interplay between the electric and magnetic fields instead of the anisotropy from the material itself, thus presenting a strong evidence of the chiral magnetic effect in the presence of gauge fields ($\mathbf{E} \cdot \mathbf{B}$ in our case). The dip in the MR curves is gradually weakened with increasing the temperature, and it completely vanishes above 200 K (Fig. 2D). In fact, the only fingerprint of the chiral anomaly available thus far in experiments is the negative MR, which has been previously reported in $\text{Bi}_{1-x}\text{Sb}_x$ (26). The reason for the observation of negative MR in Cd_3As_2 nanoplates instead of in the Cd_3As_2 bulk is the relatively low carrier density and the corresponding low Fermi level in the as-grown nanoplates (refer to fig. S6 for the quantum oscillation analysis and Hall data). This chiral magnetic effect becomes stronger in transport as the Fermi level approaches the Weyl nodes.

We note that such negative MR observed within a narrow field range alone cannot deliver a strong evidence for the existence of chiral anomaly, since MR can be affected by other factors such as crystal symmetry background or the anisotropic scattering (14, 21). In our study, however, the MOKE and the electrical measurements were independently performed, both of which corroboratively unravel the nature of the chiral anomaly in Cd_3As_2 , therefore significantly strengthening our experimental findings.

We now deal with the valley transport in Cd_3As_2 as the chiral anomaly attracts extensive attentions because it promises many intriguing transport phenomena involving the diffusion of chiral charge (e.g., the emerging valleytronics). A recent

study predicted that, with a non-zero $\mathbf{E} \cdot \mathbf{B}$ term, the charge imbalance between two valleys can diffuse across the sample. These valley charges will experience a slow relaxation process characterized by the inter-valley scattering length L_v , which is believed to be relatively long since the relaxation involves large quasi-momentum transfer or scattering between different point-group representations (14). Here, the degree of freedom of valley acts as a pseudospin index that can be effectively modulated by the electromagnetic field (14). If a detecting magnetic field is applied in the valley diffusion regime, such imbalance can be converted into a nonlocal voltage (Fig. 3A), taking the same principle as the inverse spin Hall effect (27). This nonlocal voltage follows a diffusion formula (14),

$$|V_{NL}(x)| = V_{SD} e^{-L/L_v}, \quad (2)$$

where V_{SD} is the applied source-drain voltage, L is the length between the Hall bar terminals as illustrated in Fig. 3A. From this equation, we find that the nonlocal response can survive a long distance with the weak inter-valley scattering. Nevertheless, in the case of a Dirac semimetal, the isospin relaxation will also contribute to accelerate the elimination of charge imbalance between two nodes, making it difficult to probe the valley diffusion.

To detect the nonlocal response, we employed the standard Hall-bar geometry as schematically illustrated in Fig. 3B. Nonlocal resistance R_{NL} was measured among three pairs of well-aligned “nonlocal” Hall bars (terminal 3-4, 5-6, and 7-8) at different temperature T while a constant current was applied at terminal 1-2. By sweeping \mathbf{B} which is parallel to the applied current, we measured the \mathbf{B} -dependence of R_{NL} and

the two-terminal local resistance R_L (resistance of terminal 1-2, R_{12}). Dramatically, the nonlocal resistance R_{NL} from all the nonlocal terminals (R_{34} , R_{56} , and R_{78}) adopts a complete opposite dependence on \mathbf{B} in comparison with the local resistance R_{12} . We notice that a nonlocal voltage can also be induced by the stray charge current in classical diffusive transport but it should possess the same field dependence with R_{12} . Nevertheless, in our scenario, we do expect a mixed contribution from both the Ohmic nonlocal resistance and the valley diffusion, since both of them follow the exponential damping rule (28-30). Owing to the fact that the nonlocal response from the valley diffusion vanishes at zero magnetic field, the Ohmic contribution can be precisely evaluated (28, 30) (refer to supplementary material Section VII and fig. S7 for the original data). By extracting the Ohmic contribution, the nonlocal resistance of valley transport at 100 K is shown in Fig. 3C with the corresponding local resistance displayed in the inset. As expected, a strong R_{NL} reduction is observed with the longer lateral distance.

To perform the quantitative analysis, a dimensionless coefficient α_{NL} is introduced as the strength of the nonlocal response, defined as $\alpha_{NL} = R_{NL}/R_L$. In analogy to the inverse spin Hall effect, α_{NL} arising from the valley diffusion is given by (14)

$$\alpha_{NL} = \frac{R_{NL}}{R_L} = - \left(\frac{B}{\delta + B} \right)^2 e^{-\frac{L}{L_\nu}} , \quad (3)$$

where δ is proportional to the conductance of the metal contact. It is evident that R_L and R_{NL} hold opposite sign of the field dependence (also, in agreement with the experimental data in Fig. 3C). Fig. 3D shows α_{NL} -B curves, which adopt a parabolic

dependence on the magnetic field. A tendency of saturation at high fields develops at 100 K. Such phenomenon may originate from the so-called quantum limit effect that the nonlocal response is limited by the metal contact instead of the relaxation at the sample (14). Fig. 3E plots the calculated α_{NL} as a function of temperature at given magnetic fields (9 T, 6 T, and 3 T, respectively). A slight increase of $|\alpha_{NL}|$ at low temperatures is witnessed owing to an enhanced valley diffusion process by reducing thermal fluctuations.

Importantly, L_v , a key parameter in the valley diffusive transport, can be obtained from a line fit to the semi-log plot of α_{NL} as a function of lateral length L using Eq. 3. A relatively long L_v of ~ 2 μm is extracted with a small variation against temperature (Fig. 4 inset), which is mainly attributed to a synergistic effort of high electron mobility and the suppression of electron backscattering in Dirac semimetals. By extrapolating the dependence of α_{NL} on L in Fig. 4, a high nonlocal ratio over 10% is expected for $L < 1$ μm . This high nonlocal ratio actually reveals the strong response in the mesoscopic charge distribution to the changes in chirality states, which may offer a new direction for future low-dissipation electronics.

Our work unambiguously proves the existence of the chiral anomaly in Dirac semimetals and further demonstrates the field-modulated valley transport. The ability to manipulate the chiral charge at room temperature is a significant step towards quantum electronics. The robustness of the chiral anomaly not only reflects the topological character of the Weyl nodes, but it also reveals the prospects of utilizing chiral fermions in the future valleytronic applications.

Notes: After the completion of these experiments, we became aware of the related studies reporting the observation of chiral-anomaly-induced negative MR in ZrTe_5 (31), Na_3Bi (32), and TaAs (33, 34).

Acknowledgements

This work was supported by the National Young 1000 Talent Plan, Pujiang Talent Plan in Shanghai, National Natural Science Foundation of China (61322407, 11474058), and the Chinese National Science Fund for Talent Training in Basic Science (J1103204). Part of the sample fabrication was performed at Fudan Nano-fabrication Laboratory. This work was also supported by Australian Research Council. Z-G. C. thanks QLD government for a smart state future fellowship. The Australian Microscopy & Microanalysis Research Facility and the Queensland node of the Australian National Fabrication Facility are acknowledged for providing characterization facilities. C. Z. thanks Junxue Li and Jianhui Liang for helps in the MOKE experiments.

Reference

1. R. Jackiw, N. Manton, Symmetries and conservation laws in gauge theories. *Annals of Physics* **127**, 257-273 (1980).
2. S. L. Adler, Axial-vector vertex in spinor electrodynamics. *Physical Review* **177**, 2426 (1969).
3. J. S. Bell, R. Jackiw, A PCAC puzzle: $\pi 0 \rightarrow \gamma\gamma$ in the σ -model. *Il Nuovo Cimento A* **60**, 47-61 (1969).
4. H. B. Nielsen, M. Ninomiya, The Adler-Bell-Jackiw anomaly and Weyl fermions in a crystal. *Physics Letters B* **130**, 389-396 (1983).
5. X. Wan, A. M. Turner, A. Vishwanath, S. Y. Savrasov, Topological semimetal and Fermi-arc surface states in the electronic structure of pyrochlore iridates. *Physical Review B* **83**, 205101 (2011).
6. P. Hosur, X. Qi, Recent developments in transport phenomena in Weyl semimetals. *Comptes Rendus Physique* **14**, 857-870 (2013).
7. A. Burkov, M. Hook, L. Balents, Topological nodal semimetals. *Physical Review B* **84**, 235126 (2011).
8. S. M. Young *et al.*, Dirac Semimetal in Three Dimensions. *Physical Review Letters* **108**, 140405 (2012).
9. Z. Wang *et al.*, Dirac semimetal and topological phase transitions in A_3Bi ($\text{A}=\text{Na, K, Rb}$). *Physical Review B* **85**, 195320 (2012).

10. Z. Wang, S.-C. Zhang, Chiral anomaly, charge density waves, and axion strings from Weyl semimetals. *Physical Review B* **87**, 161107 (2013).
11. S.-C. Zhang, J. Hu, A four-dimensional generalization of the quantum Hall effect. *Science* **294**, 823-828 (2001).
12. D. Son, B. Spivak, Chiral anomaly and classical negative magnetoresistance of Weyl metals. *Physical Review B* **88**, 104412 (2013).
13. A. Burkov, Anomalous Hall Effect in Weyl Metals. *Physical review letters* **113**, 187202 (2014).
14. S. Parameswaran, T. Grover, D. Abanin, D. Pesin, A. Vishwanath, Probing the Chiral Anomaly with Nonlocal Transport in Three-Dimensional Topological Semimetals. *Physical Review X* **4**, 031035 (2014).
15. Z. Wang, H. Weng, Q. Wu, X. Dai, Z. Fang, Three-dimensional Dirac semimetal and quantum transport in Cd 3 As 2. *Physical Review B* **88**, 125427 (2013).
16. Z. K. Liu *et al.*, Discovery of a three-dimensional topological Dirac semimetal, Na3Bi. *Science* **343**, 864-867 (2014).
17. S. Borisenko *et al.*, Experimental Realization of a Three-Dimensional Dirac Semimetal. *Physical Review Letters* **113**, 027603 (2014).
18. M. Neupane *et al.*, Observation of a three-dimensional topological Dirac semimetal phase in high-mobility Cd3As2. *Nature communications* **5**, (2014).
19. Z. K. Liu *et al.*, A stable three-dimensional topological Dirac semimetal Cd3As2. *Nature materials* **13**, 677-681 (2014).
20. S.-Y. Xu *et al.*, Observation of Fermi arc surface states in a topological metal. *Science* **347**, 294-298 (2015).
21. T. Liang *et al.*, Ultrahigh mobility and giant magnetoresistance in the Dirac semimetal Cd3As2. *Nature materials* **14**, 280-284 (2014).
22. J. Cao *et al.*, Landau level splitting in Cd3As2 under high magnetic fields. *arXiv preprint arXiv:1412.0824*, (2014).
23. P. Hosur, X.-L. Qi, Tunable circular dichroism due to the chiral anomaly in Weyl semimetals. *Physical Review B* **91**, (2015).
24. Z. Q. Qiu, S. D. Bader, Surface magneto-optic Kerr effect. *Review of Scientific Instruments* **71**, 1243 (2000).
25. E. Zhang *et al.*, Magnetotransport properties of Cd3As2 nanostructures. *arXiv preprint arXiv:1503.00422*, (2015).
26. H.-J. Kim *et al.*, Dirac versus Weyl Fermions in Topological Insulators: Adler-Bell-Jackiw Anomaly in Transport Phenomena. *Physical Review Letters* **111**, (2013).
27. T. Kimura, Y. Otani, T. Sato, S. Takahashi, S. Maekawa, Room-temperature reversible spin Hall effect. *Physical review letters* **98**, 156601 (2007).
28. R. Gorbachev *et al.*, Detecting topological currents in graphene superlattices. *Science* **346**, 448-451 (2014).
29. C. Brüne *et al.*, Evidence for the ballistic intrinsic spin Hall effect in HgTe nanostructures. *Nature Physics* **6**, 448-454 (2010).
30. D. Abanin *et al.*, Giant nonlocality near the Dirac point in graphene. *Science* **332**, 328-330 (2011).
31. Q. Li *et al.*, Observation of the chiral magnetic effect in ZrTe5. *arXiv preprint arXiv:1412.6543*, (2014).

32. J. Xiong *et al.*, Signature of the chiral anomaly in a Dirac semimetal: a current plume steered by a magnetic field. *arXiv preprint arXiv:1503.08179*, (2015).
33. C. Zhang *et al.*, Observation of the Adler-Bell-Jackiw chiral anomaly in a Weyl semimetal. *arXiv preprint arXiv:1503.02630*, (2015).
34. X. Huang *et al.*, Observation of the chiral anomaly induced negative magneto-resistance in 3D Weyl semi-metal TaAs. *arXiv preprint arXiv:1503.01304*, (2015).

FIGURES

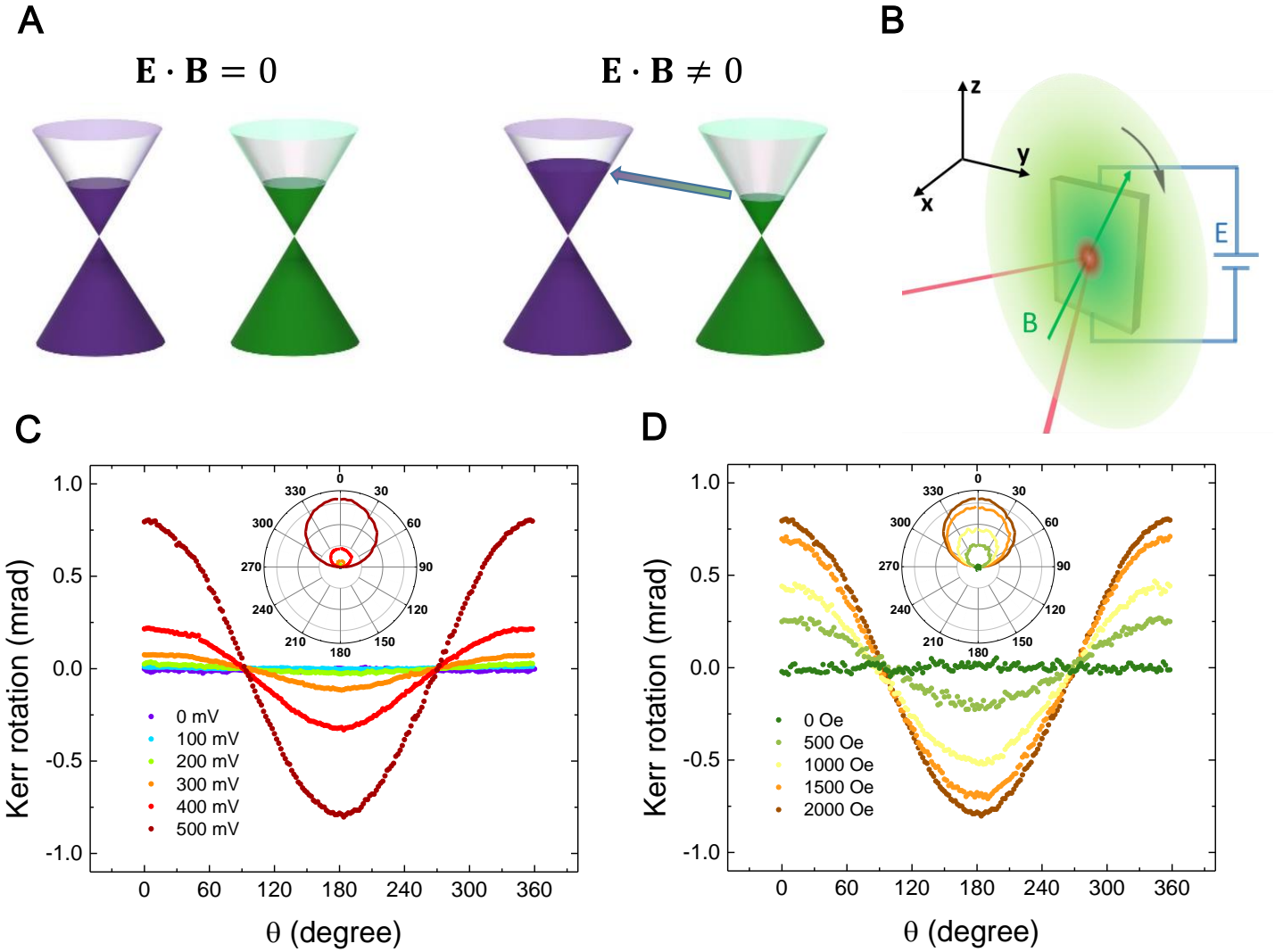


Fig. 1. Illustration of the charge pumping process and ROTMOKE data of the Cd_3As_2 bulk crystals. (A) Charge pumped from one Weyl node to the other in the presence of chiral gauge fields. This pumping process is also applied to Dirac semimetals, whose nodes are degenerated but distinguished by isospin. (B) Schematic drawing of the MOKE experiment set-up. The magnetic field is rotated in the y - z plane, parallel to the sample surface. A constant electric bias was applied across the sample. The incident laser is p -polarized with a wavelength of 670 nm. (C and D) ROTMOKE signals of the Cd_3As_2 crystals under different electric bias and magnetic field, adopting a cosine-function dependence on θ . Here θ is defined as the angle between \mathbf{E} and \mathbf{B} . For (C) the magnetic field was fixed at 2000 Oe and for (D) the bias is fixed at 500 mV. The insets are the data plotted in the polar coordinates.

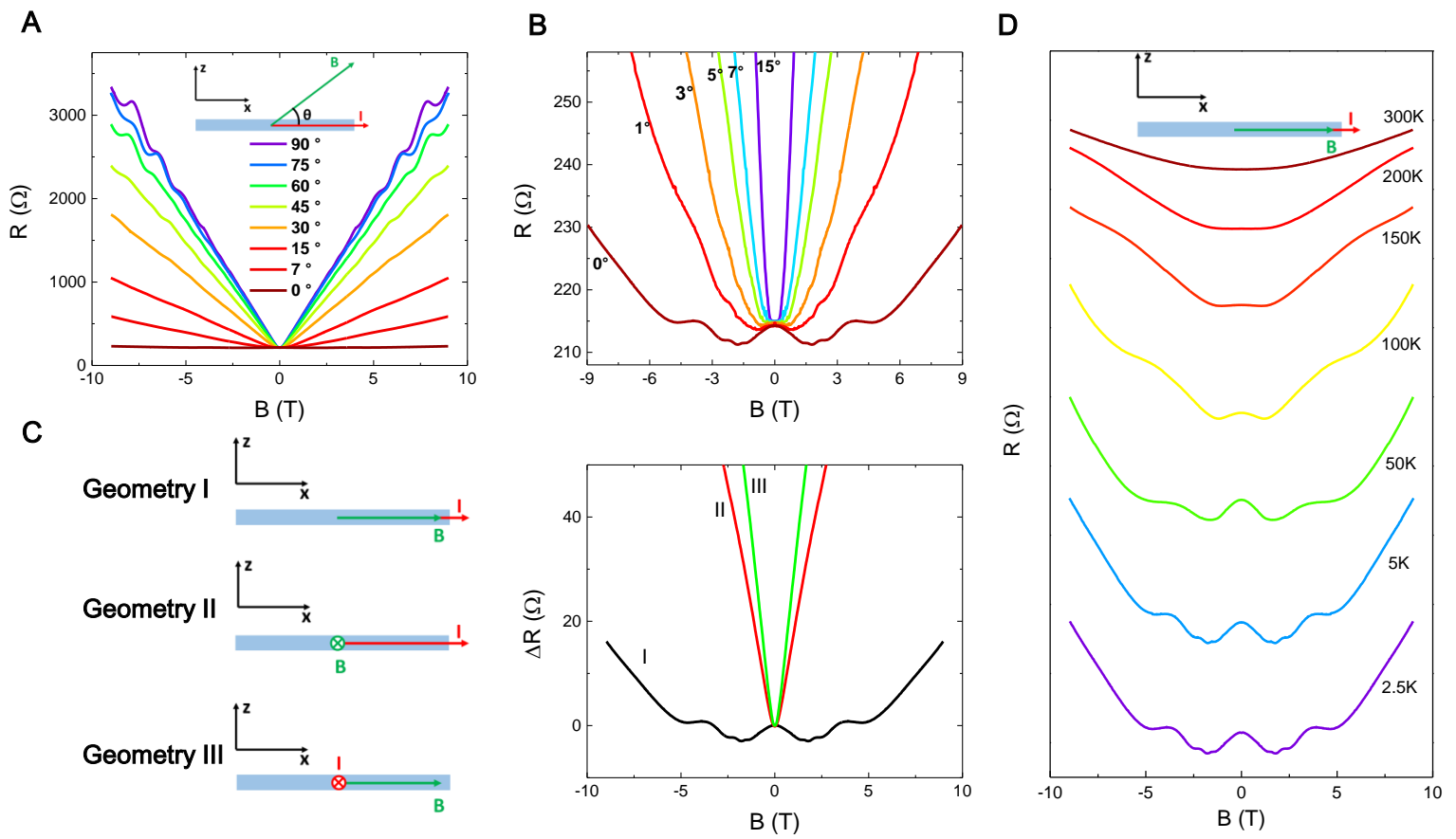


Fig. 2. Chiral anomaly induced negative MR from the Cd₃As₂ nanoplates. (A) The angle-dependent MR curves. The inset is the schematic view of the transport measurement setup, showing **B** rotating in the x-z plane and θ defined as the angle between **B** and **I**. For a large θ , the sample exhibits a positive **B**-linear MR. (B) An enlarged view of MR as θ approaches zero. MR decreases rapidly as θ approaches zero. When θ is near zero, a clear dip was observed in the -2~2 T range, followed by an upturn of MR in the larger fields. (C) MR in three different geometries in transport measurements at 2.5 K. The negative MR only appears when **E** is parallel with **B**. The control experiments exclude the crystal anisotropy effect on the observed negative MR. (D) Stack view of MR at different temperatures when **E** is parallel with **B**. The dip in the MR curves is weakened as the temperature increases and it completely vanishes above 200 K.

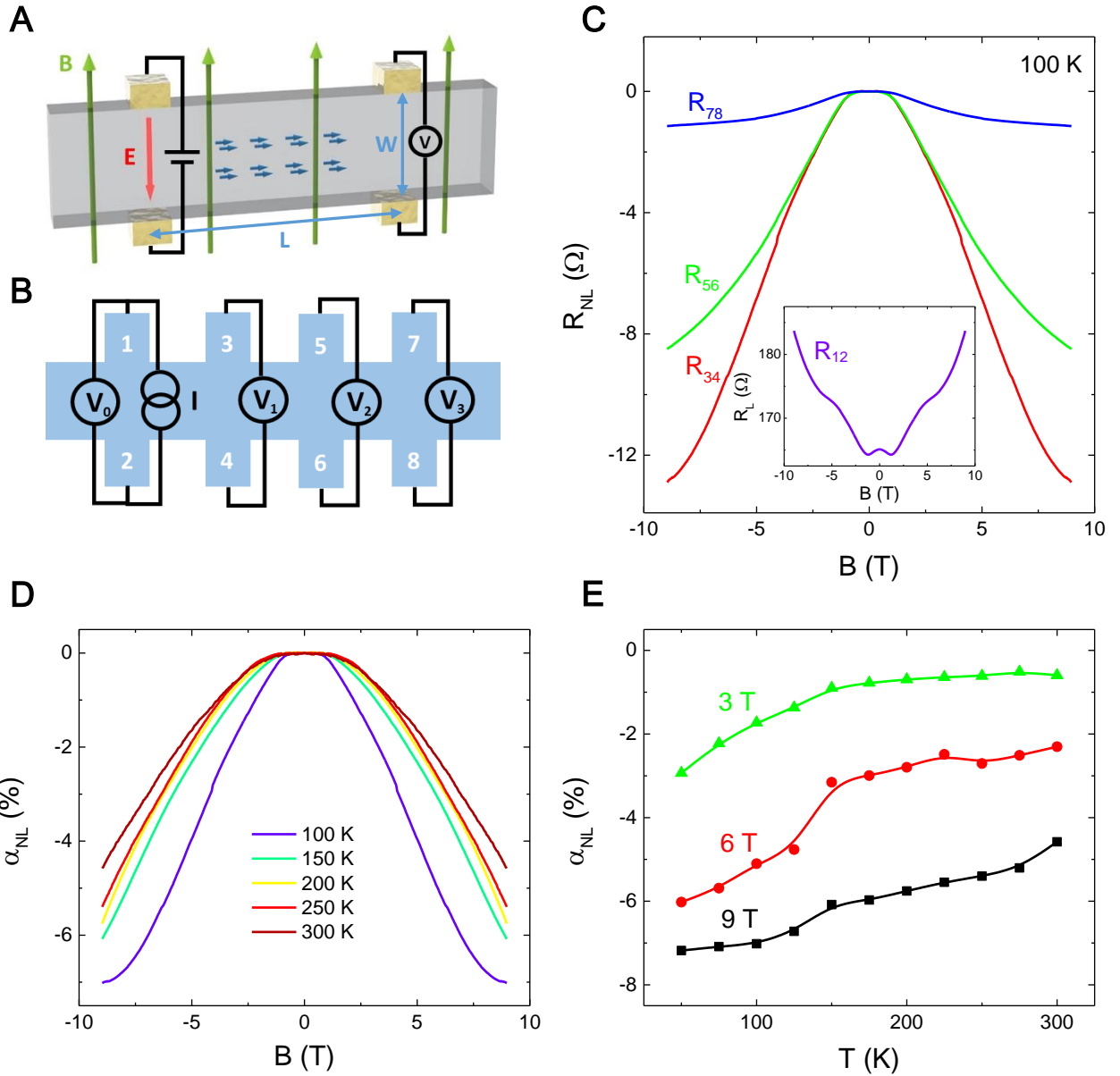


Fig. 3. Detection of valley transport in the Cd_3As_2 nanoplates. (A) Schematic view of the valley diffusion process. Parallel (antiparallel) electric and magnetic fields generate the charge imbalance between two Weyl nodes due to the chiral anomaly. The charge imbalance of different valleys can diffuse across the sample and can be converted into a nonlocal voltage along the applied magnetic field direction. (B) Schematic view of the nonlocal resistance measurement in a Hall-bar-geometry device with three pairs of nonlocal channels. (C) The extracted nonlocal resistance R_{NL} (R_{34} , R_{56} , and R_{78}) measured in the Hall bar geometry at 100 K. The inset is R_L - \mathbf{B} curves from terminal 1-2. (D) The nonlocal ratio α_{NL} - \mathbf{B} curves at different temperatures. (E) α_{NL} as a function of temperature at 9 T, 6 T, and 3 T, respectively. A slight increase of $|\alpha_{NL}|$ at low temperatures is witnessed.

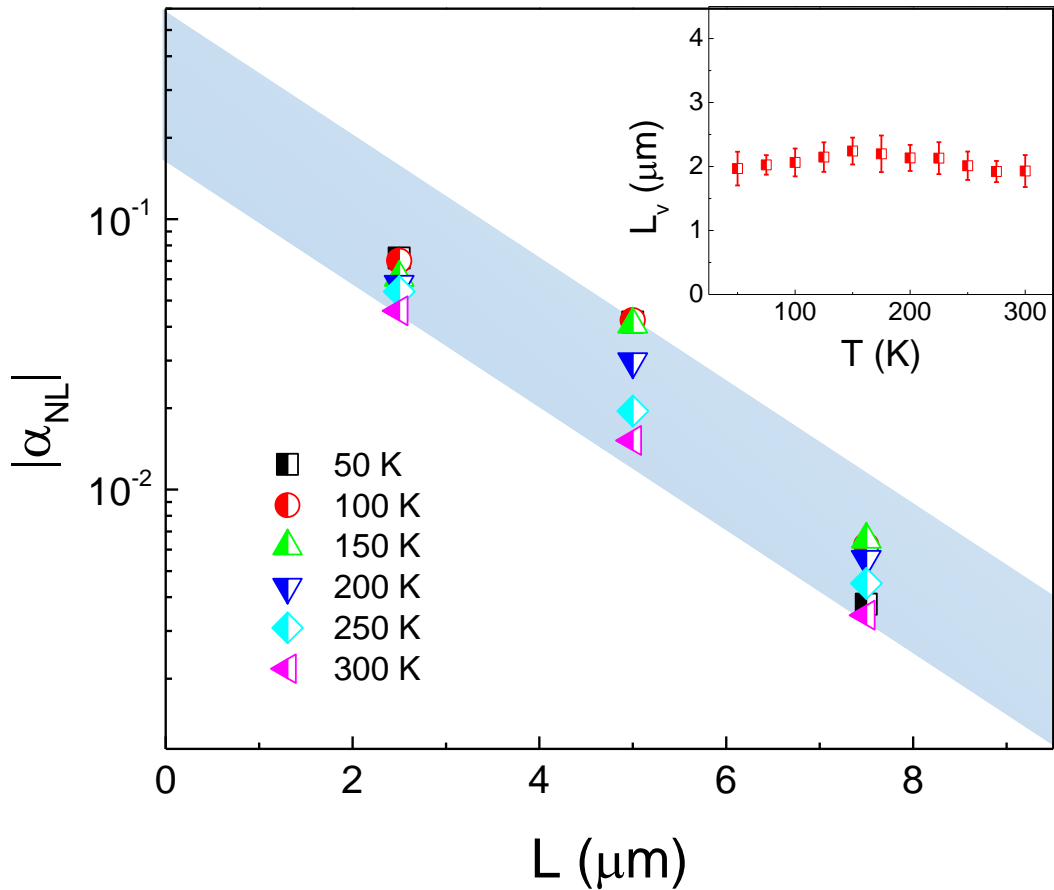


Fig. 4. Length dependence and calculated valley-relaxation length of the valley transport. (A)

The calculated $|\alpha_{NL}|$. It decays exponentially with the increasing of lateral length L . (B) The calculated valley-relaxation length L_v at different temperatures.

Supporting Online Material for Detection of chiral anomaly and valley transport in Dirac semimetals

Cheng Zhang, Enze Zhang, Yanwen Liu, Zhi-Gang Chen*, Sihang Liang, Junzhi Cao,

Xiang Yuan, Lei Tang, Qian Li, Teng Gu, Yizheng Wu, Jin Zou*, Faxian Xiu*

* Correspondence and requests for materials should be addressed to F. X. (E-mail: faxian@fudan.edu.cn), J. Z. (Email: j.zou@uq.edu.au) and Z-G. C. (Email: z.chen1@uq.edu.au)

This file includes:

I. Bulk Cd₃As₂ crystal growth method and crystal structure

II. Magneto-optical Kerr effect (MOKE) of Cd₃As₂ bulk crystal

III. Theoretical interpretation for the chiral anomaly induced circular dichroism

IV. Electrical transport properties of Cd₃As₂ bulk crystal

V. Synthesis and structural characterizations of Cd₃As₂ nanoplates

VI. Low carrier density in as-grown Cd₃As₂ nanoplates

VII. Extracting the Ohmic resistance from the original data

VIII. Valley-relaxation length from field dependence of nonlocal ratio

IX. Another set of nonlocal transport data

References

I. Bulk Cd₃As₂ crystal growth method and crystal structure

High-quality Cd₃As₂ single crystals were synthesized by self-flux growth method in a tube furnace with stoichiometric amounts of high-purity Cd powder (4N) and As powder (5N). Mixed elements were sealed in an alumina crucible inside an iron crucible under argon atmosphere. The iron crucible was heated to 800-900°C and kept for 24 hours, then slowly cooled down to 450°C at 6°C/hour. Then the crucible was kept at 450°C for more than one day before cooled naturally to room temperature. The superfluous Cd flux was removed by centrifuging in a vacuum quartz tube at 450°C.

The as-grown single crystal Cd₃As₂ adopts {112} crystal planes (Fig. S1A) with a large shining surface, which is perfect for obtaining a large reflection signal during the experiment. Fig. S1B is a typical high-resolution transmission electron microscopy (TEM) image of a Cd₃As₂ thin flake on a holey carbon grid with the selected area electron diffraction (SAED) pattern (top left) and a low magnification TEM picture (top right) in the inset. From the index of SAED pattern, the crystal structure of our sample is found to be I4₁/acd structure. It has a distorted superstructure of the antifluorite structure, whose unit cell is tetragonal with $a=12.633(3)$ Å and $c=25.427(7)$ Å. Each unit cell contains 96 Cd atoms and 64 As atoms.

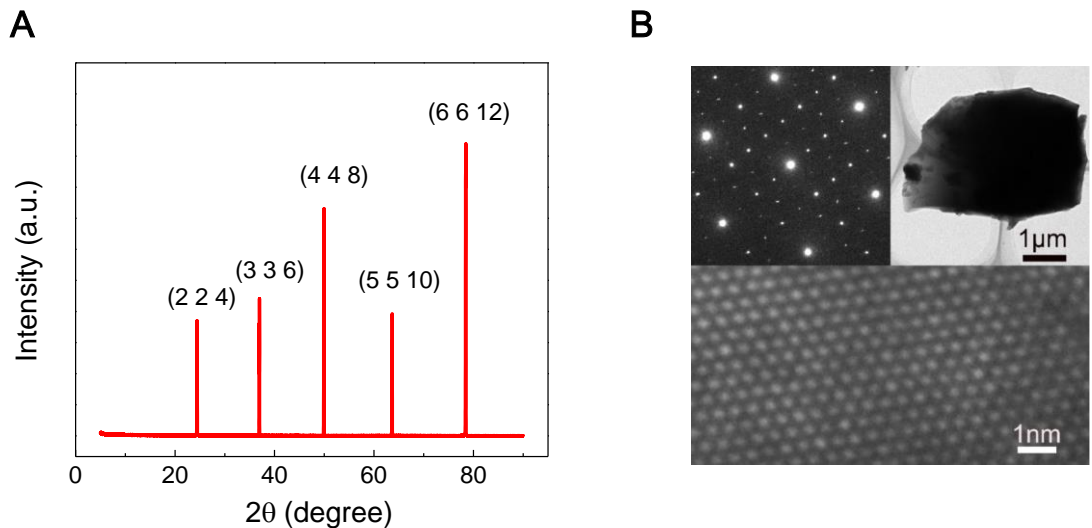


Fig. S1. Structural characterizations of Cd_3As_2 bulk crystal. (A) A typical X-ray diffraction patterns of the single crystal Cd_3As_2 with (112) surface. (B) A high-resolution TEM image of a Cd_3As_2 flake on a holey carbon grid with the selected area diffraction pattern (top left) and a low magnification TEM picture (top right) in the inset.

II. Magneto-optical Kerr effect (MOKE) of Cd_3As_2 bulk crystal

For comparison, we also performed rotating-of-field magneto-optical Kerr effect (ROTMOKE) measurements on the Cd_3As_2 bulk single crystal with the magnetic field fixed in the x-z plane. Two kinds of measurement configurations were adopted, in which the applied electric bias was parallel with and perpendicular to the x-z plane, respectively. In the former case, similar 360 °-period ROTMOKE curves was observed (Fig. S2C), consistent with the angular dependence of $\mathbf{E} \cdot \mathbf{B}$ chiral gauge field. However, when the bias was added perpendicularly to the B-rotating plane, *i.e.* $\mathbf{E} \cdot \mathbf{B}$ became zero, no Kerr signal was detected (Fig. S2D). These results totally isolate the detected Kerr signals from the conventional magnetic order.

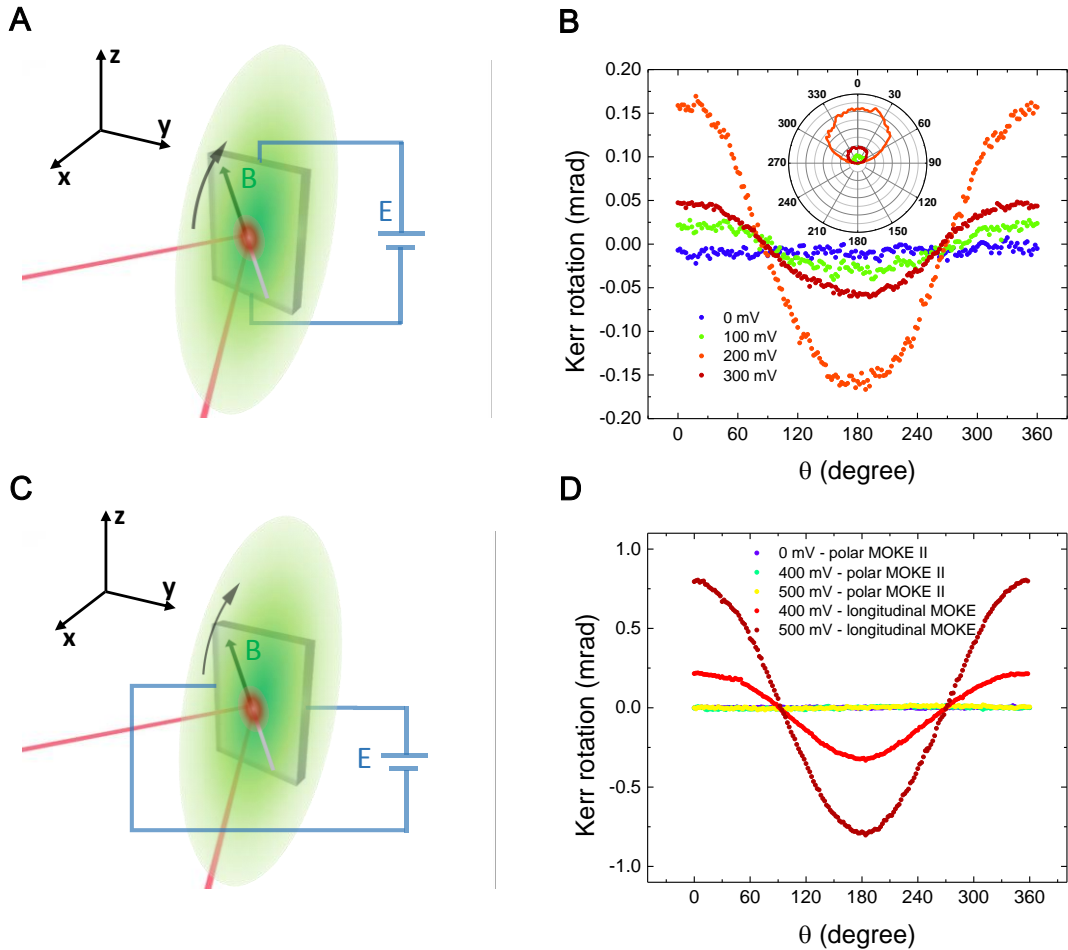


Fig. S2. Comparisons of the ROTMOKE data of Cd₃As₂ bulk crystal in different measurement configurations. (A) Schematic ROTMOKE I set-up. The magnetic field **B** is rotated in the x-z plane. A constant electric bias was applied in the **B**-rotating plane. The laser is horizontally polarized with a wavelength of 670 nm. (B) ROTMOKE signals of Cd₃As₂ crystal under different electric bias and magnetic field, adopting a cosine-function dependence on θ . Here θ is defined as the angle between the electric and magnetic field. For (B) the magnetic field is fixed at 2000 Oe. The insets are data plotted in polar coordinates. (C) Schematic view of the ROTMOKE II set-up. The only difference between ROTMOKE I and II is the direction of the electric bias. Here, **E** is perpendicular to **B**-rotating plane. (D) Comparison of the ROTMOKE data from the main text with the data from the ROTMOKE II set-up. The magnetic field was fixed at 2000 Oe. No Kerr rotation was observed in the ROTMOKE II configuration.

Meanwhile, the magneto-optical Kerr effect (MOKE) experiments on the sample with electric bias were performed to explore the magnetic-field dependence of the Kerr signals. Firstly, we fixed the bias voltage to be 500 mV and swept the in-plane magnetic field back and forth at one certain direction in the y-z plane. The obtained longitudinal MOKE signals show a quasi-linear relationship with the magnetic field but retain a distinct hysteresis during the sweeping process (Fig. S3). The quasi-linear behavior has no sign of saturation in our field range. The hysteresis is not affected by the sweeping speed or the sampling interval. By changing the sweeping field direction, we reproduced the angular-dependent Kerr rotation. The Kerr signals remain non-saturated with hysteresis which vanishes when the magnetic field is perpendicular to the electric field. Conventionally, the hysteresis in the longitudinal Kerr signal is

associated with ferromagnetic order. However, in our case, clearly no magnetic element is involved. The longitudinal MOKE stays non-saturated at all angles in our field range of between -3000 and 3000 Oe, inconsistent with the scenario of spin flipping under external fields. The observed anomalous hysteresis is beyond the current understanding and requires further investigations.

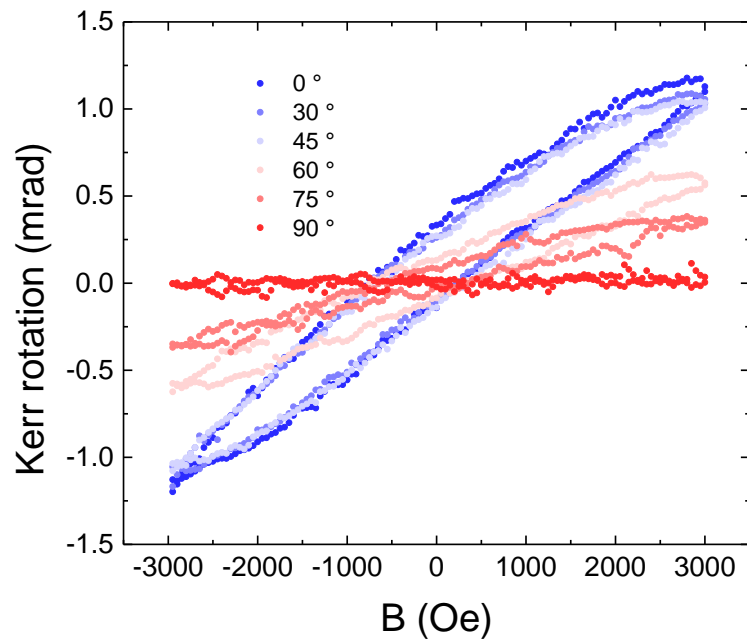


Fig. S3. MOKE data of Cd_3As_2 bulk crystal. MOKE signals of Cd_3As_2 crystal at different magnetic field directions. The measurements adopt the geometry from the main text (Fig. 1B).

III. Theoretical interpretation for the chiral anomaly induced circular dichroism

Systems with nonzero γ possess circular dichroism, which can convert a linearly polarized light into elliptical polarization as light going through. The eigenvalue of the resulted dielectric tensor can be written as $n_{L,R}^2(\omega) = \epsilon_0(\omega) \pm \gamma q$, where q and ω are the wave vector and frequency of the light. If $\text{Im}(n_L) \neq \text{Im}(n_R)$, the two circular polarizations would get different absorptions, leading to circular dichroism. The ellipticity of the obtained light is given by $|\tan \theta_{CD}| = \left| \frac{E_R - E_L}{E_R + E_L} \right| \approx \frac{|\text{Im}[\gamma]| l \omega^2}{2c^2}$, if $|\frac{\gamma \omega}{c}| \ll \epsilon_0$ (1). Here l is the sample thickness, c is the light speed, and $E_{R,L}$ are the transmitted amplitudes of the circularly polarized fields.

The semi-classical equations of motion for a wave packet with band dispersion $\epsilon(\mathbf{k})$ and Berry curvature $F(\mathbf{k})$ is $\dot{r} = \mathbf{v}(\mathbf{k}) - F(\mathbf{k}) \times \frac{e}{\hbar} \mathbf{E}(\mathbf{r}, t)$, $\dot{k} = \frac{e}{\hbar} \mathbf{E}(\mathbf{r}, t)$, where $\mathbf{v}(\mathbf{k}) = \nabla_k \epsilon(\mathbf{k})$, e is the electron charge and \hbar is the reduced Planck constant. The second term describes an anomalous Hall current if integrating over \mathbf{k} . The total Hall current density is given by $J_{Hall}(\mathbf{r}, t) \approx \frac{e^2}{\hbar} \mathbf{E}(\mathbf{r}, t) \int_k F_k (1 + i \mathbf{q} \cdot \mathbf{v}_k t)$. Thus, the non-vanishing part of γ , proportional to the \mathbf{q} -linear part of the Hall conductivity, can be summarized as $\gamma = \frac{e^2}{\hbar} \frac{i\tau}{\epsilon_0 \omega} \int_k (F_k \cdot \mathbf{q})(\mathbf{q} \cdot \mathbf{v}_k)$. τ is intra-valley scattering time. For a two-Weyl-node system, $\gamma = \frac{e^2}{3\pi^2 \hbar^2} \frac{i\tau}{\epsilon_0 \omega} \left(\frac{3e^2 \hbar v_F^3}{2} \mathbf{E} \cdot \mathbf{B} \tau_{inter} \right)$ with τ_{inter} the inter-valley scattering time. The above theoretical analysis is adopted from ref (1).

IV. Electrical transport properties of Cd_3As_2 bulk crystal

Standard magnetoresistance measurements were conducted to probe the transport properties of Cd_3As_2 single crystal. A constant current was applied within the (112) atomic planes while the magnetic field was tilted from perpendicular to parallel to the (112) planes. Strong anisotropy magnetoresistance and quantum oscillations were clearly resolved at low temperatures. The ρ_{xx} -T curve describes a typical metallic behavior owing to the semimetal band structure, consistent with previous reports (2).

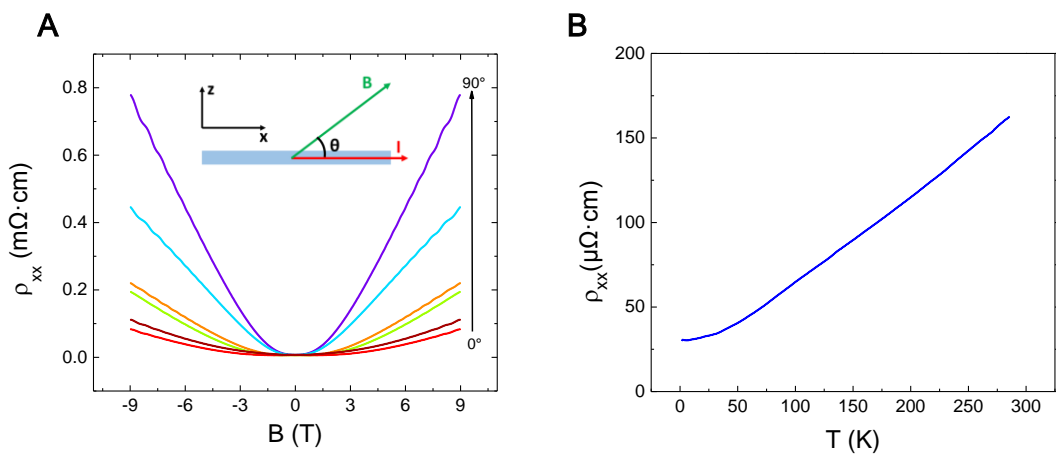


Fig. S4. Electrical transport properties of Cd_3As_2 bulk crystal. (A) The angular dependence of longitudinal resistivity at 3 K. The Shubnikov-de Haas oscillations are observed at different angles. (B) The longitudinal resistivity as a function of temperature.

V. Synthesis and structural characterizations of Cd₃As₂ nanoplates

The Cd₃As₂ nanoplates were grown using Cd₃As₂ powders as the precursor in a horizontal tube furnace, in which Argon was a carrier gas. Prior to the growth, the furnace was pumped and flushed with Argon several times to remove water and oxygen. The temperature was ramped to the growth temperature within 15 min, held constantly for 20 min, and then was cooled down naturally over ~2 h in a constant flow of argon before the substrates were removed at room-temperature. The precursor boat was placed in the hot center of the furnace (held at 720 °C), while the smooth quartz substrates were placed in the down-stream within a very small temperature range from 150 °C to 200 °C. The smooth quartz substrates then appeared shining to the naked eyes.

The crystal structures of the synthesized products were characterized by X-ray diffraction (XRD), recorded on an X-ray diffractometer equipped with graphite monochromatized, Cu K α radiation ($\lambda = 1.5418 \text{ \AA}$). The morphological, structural, and chemical characteristics of the synthesized products were investigated by scanning electron microscopy (SEM, JEOL 7800 and 7001) and transmission electron microscopy (TEM, FEI F20) equipped with energy-dispersive X-ray spectroscopy (EDS).

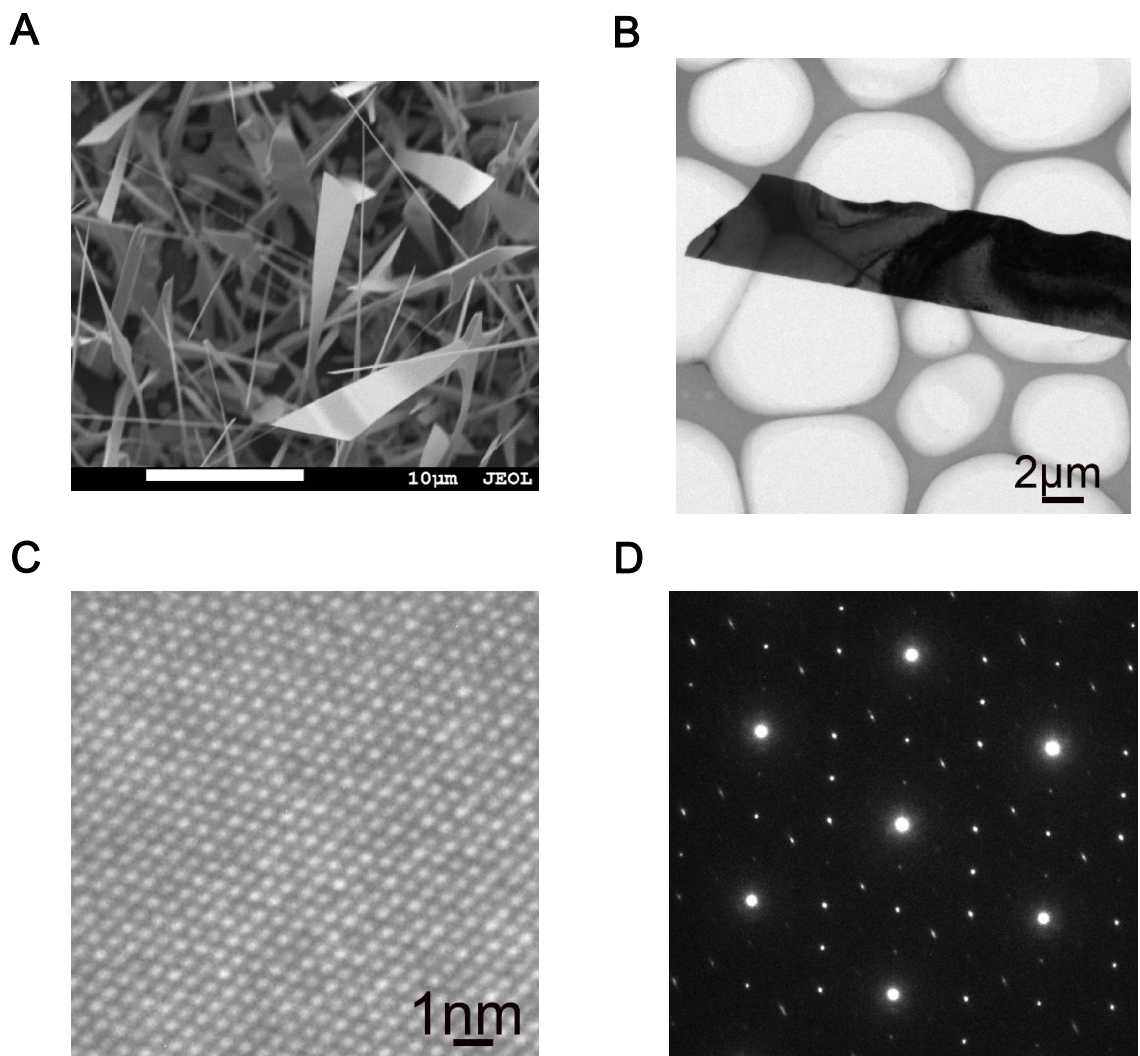


Fig. S5. Structural characterizations of Cd_3As_2 nanoplates. (A) A Typical SEM image of the as-grown Cd_3As_2 nanoplates. (B) A TEM image of a Cd_3As_2 nanoplate on a holey carbon grid. (C) High-resolution TEM picture revealing a perfect crystalline structure. (D) The corresponding SAED pattern.

VI. Low carrier density in as-grown Cd₃As₂ nanoplates

Quantum oscillation can give detailed information of the carrier and Fermi surface. During the transport measurement, clear Shubnikov-de Haas (SdH) oscillations were resolved at low temperatures owing to the high mobility of the as-grown Cd₃As₂ nanoplates (Fig. S6A). Fermi wave vector k_F , was determined to be 0.032 \AA^{-1} , revealing a relatively low Fermi level. Fig. S4B depicts the Hall resistance of Cd₃As₂. By analyzing the Hall data, the low carrier density also agrees with the detected small Fermi wave vector. Chiral magnetic effect can be significantly enhanced in the system with Fermi level close to the Weyl point. The low carrier density of our samples enables us to observe the negative magnetoresistance which was not accessible in previous studies with high-carrier-density samples.

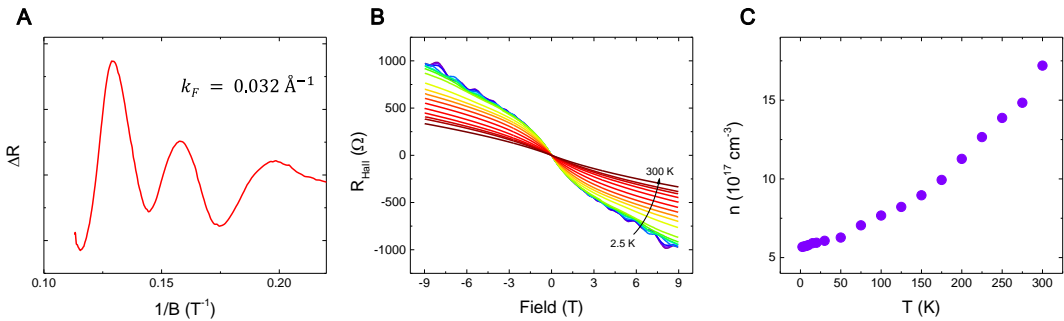


Fig. S6. SdH oscillation and Hall data of the Cd₃As₂ nanoplates. (A) Extracted SdH oscillations, showing a uniform periodicity against $1/B$. (B) Hall data of the samples. (C) Calculated carrier density as a function of temperature from Hall effect.

VII. Extracting the Ohmic resistance from the original data

In order to extract the stray charge currents from the detected nonlocal signal, we use van der Pauw formula $R_{NL} = \frac{\rho}{\pi} e^{-\pi L/W}$ to calculate the Ohmic resistance (3, 4), where resistivity $\rho = R_L W/L$. W and L are defined in Fig. 2A in the main text. Fig. S7B is the original data for the detected nonlocal resistance, which is mixed with valley diffusion and Ohmic resistance. By plotting the zero field resistance which has pure Ohmic contribution, we find that it also adopts an exponential decay with L . Moreover, we measured the nonlocal resistance under a perpendicular magnetic field. Under this condition, the detected nonlocal resistance adopts an identical field dependence in semi-log plot. It implies that it is reasonable to apply the van der Pauw formula for Ohmic resistance in our study.

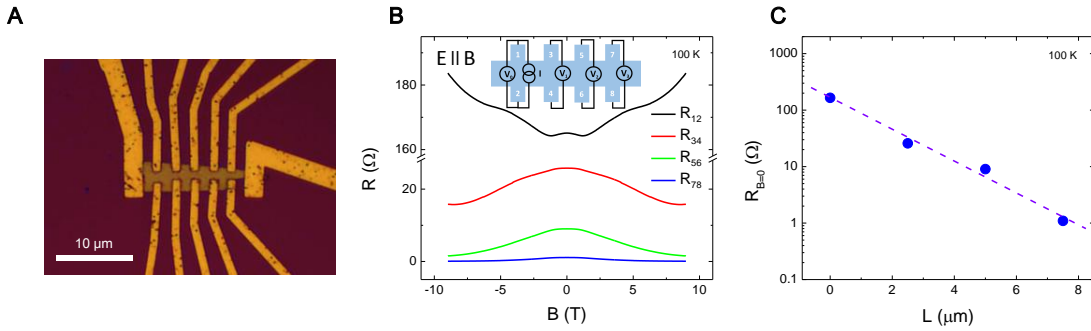


Fig. S7. Ohmic contribution in nonlocal transport in Cd_3As_2 nanoplates. (A) The optical picture of the Cd_3As_2 nanoplate device with three pairs of Hall bars, the same device that we used to obtain the nonlocal transport data in the main text. (B) Original measured nonlocal resistance R_{NL} (R_{34} , R_{56} , and R_{78}) and local resistance R_L (R_{12}). The zero field resistance follows an exponential decay with L but it adopts an opposite B dependence for R_L and R_{NL} .

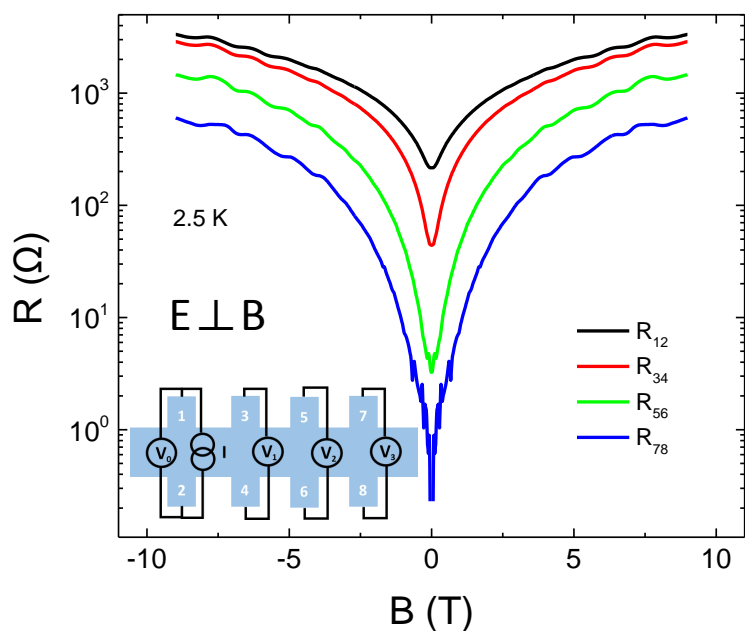


Fig. S8. Pure Ohmic resistance in nonlocal transport in Cd_3As_2 nanoplates. The detected pure Ohmic resistance is achieved by eliminating the valley transport under the perpendicular electric and magnetic fields. The nonlocal resistance here follows an exponential decay with L at all field range.

VIII. Valley-relaxation length from field dependence of nonlocal ratio

Valley-relaxation length L_v can also be fitted from the magnetic field dependence of the nonlocal ratio α_{NL} . The nonlocal response arising from valley diffusion is given by(5)

$$\alpha_{NL} = \frac{R_{NL}}{R_L} = - \left(\frac{B}{\delta + B} \right)^2 e^{-\frac{L}{L_v}} , \quad (1)$$

where δ is proportional to the conductance of the metal contact. For simplicity, we assume that $1/\delta$ is scaled linearly with the magnetic field B based on the facts observed from the most conventional metals. Remarkably, the fitted curves perfectly match the experimental results as shown in Fig. S9A. The calculated L_v adopts a similar temperature dependence as the one fitted from the length scaling but with a slightly smaller value. These similar results verify the calculated L_v .

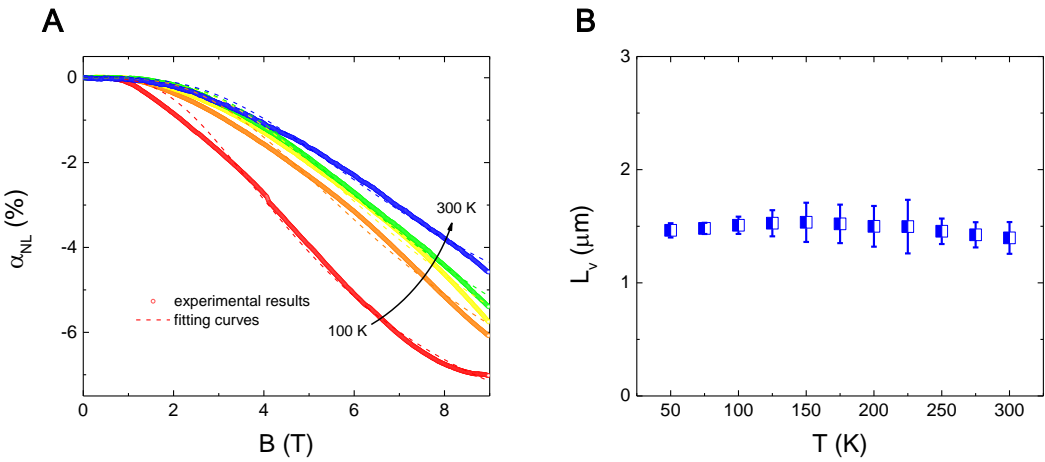


Fig. S9. Fitting curves and calculated parameters of the nonlocal transport. (A) Fittings of the α_{NL} - B curves at different temperatures. (B) Calculated L_v at different temperatures.

IX. Another set of nonlocal transport data

To ensure the reproducibility of the results, we show another set of nonlocal transport data obtained from the second sample. Similar nonlocal signal was detected in this sample. However, the negative magnetoresistance is not observed and the nonlocal ratio α_{NL} is much smaller than the one shown in the main text. By performing the Hall effect and quantum oscillation measurements, we find that the carrier density and Fermi wave vector is relatively large in this sample. The large difference between samples with different Fermi level reveals the importance of high quality and low carrier density for the detection of chiral anomaly.

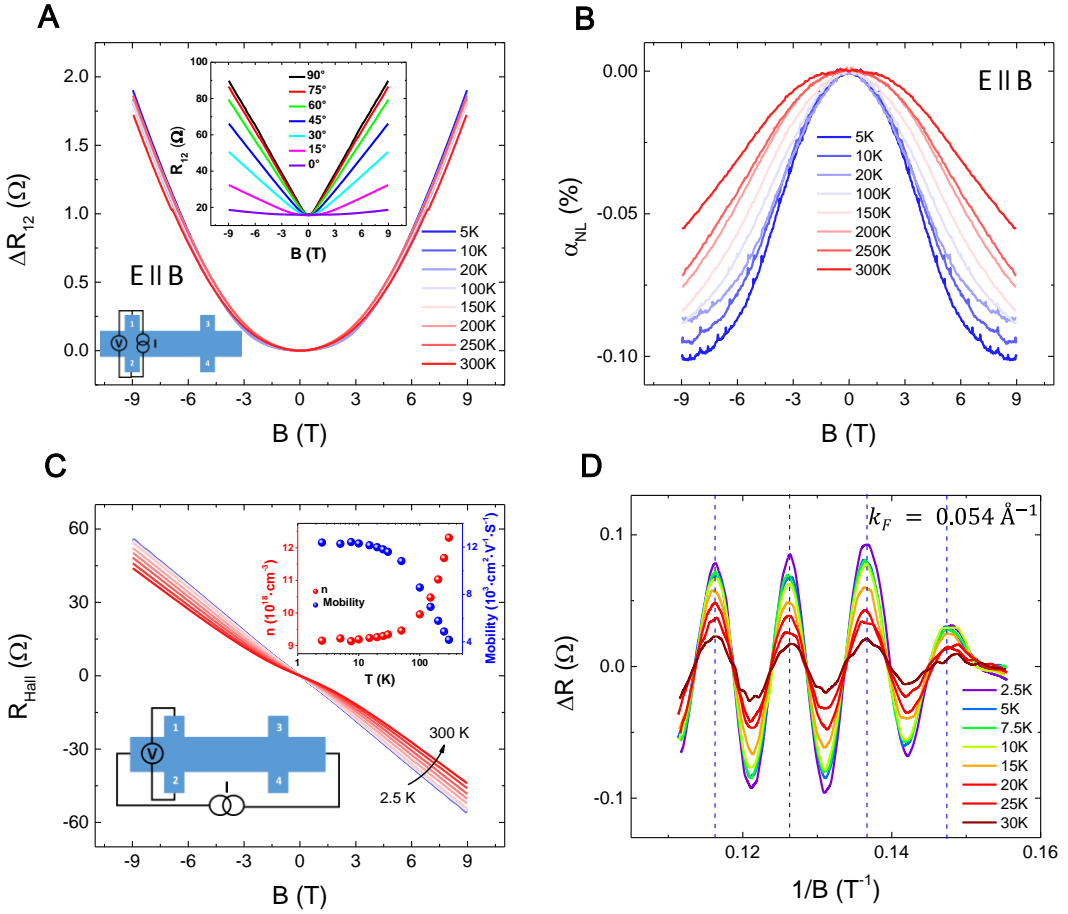


Fig. S10. Nonlocal transport of another sample. (A) $\Delta R_L = R_L(B, T) - R_L(0, T)$ measured in a two-terminal configuration. The inset in the angular dependence of R_L - \mathbf{B} curves with θ defined as the angle between the applied current and the magnetic field. $\theta = 90^\circ$ represents that \mathbf{B} is perpendicular to the sample. (B) Measured nonlocal response α_{NL} - \mathbf{B} curves at different temperatures with α_{NL} being the ratio between R_{NL} and R_L . (C) Hall data of the sample when $\theta = 90^\circ$ with calculated carrier density n and mobility shown in the inset. (D) Extracted SdH oscillation curves, showing a uniform periodicity against $1/B$.

Reference

1. P. Hosur, X.-L. Qi, Tunable circular dichroism due to the chiral anomaly in Weyl semimetals. *Physical Review B* **91**, (2015).
2. T. Liang *et al.*, Ultrahigh mobility and giant magnetoresistance in the Dirac semimetal Cd₃As₂. *Nature materials* **14**, 280-284 (2014).
3. D. Abanin *et al.*, Giant nonlocality near the Dirac point in graphene. *Science* **332**, 328-330 (2011).
4. R. Gorbachev *et al.*, Detecting topological currents in graphene superlattices. *Science* **346**, 448-451 (2014).
5. S. Parameswaran, T. Grover, D. Abanin, D. Pesin, A. Vishwanath, Probing the Chiral Anomaly with Nonlocal Transport in Three-Dimensional Topological Semimetals. *Physical Review X* **4**, 031035 (2014).